Journal of Applied Fluid Mechanics, Vol. 16, No. 7, pp. 1442-1454, 2023.
Available online at www.jafmonline.net, ISSN 1735-3572, EISSN 1735-3645.
https://doi.org/10.47176/jafm.16.07.1690

Study on Pressure Reconstruction Method of Explosion Shock Wave

L. Wang† and D. Kong

School of Mechanical Engineering, Nanjing University of Science and Technology, Jiangsu Nanjing, Jiangsu 210094, China

†*Corresponding Author Email: 2223263181@qq.com*

(Received December 3, 2022; accepted March 9, 2023)

ABSTRACT

Shock waves are one of the primary damage parameters of an ammunition explosion. Therefore, accurately obtaining the shock wave pressure distribution law after ammunition explosion is greatly significant for the ammunition damage power evaluation and the guidance of ammunition selection in the operations course. This study established the mapping function between the surface reflected and free-field shock wave pressures, considering the altitude effect on shock wave pressure. Finite element numerical simulation analysis of typical (trinitrotoluene) TNT explosive quality and static explosion shock wave pressure test were performed, and the model calculation accuracy was verified by using the obtained shock wave pressure data. The Validation results show that the model had 84% calculation accuracy and could well reflect the explosion shock wave pressure distribution law. Furthermore, the results provided a new calculation method and scientific data support for the accurate evaluation of the damage power of an ammunition explosion. Additionally, the results are significant for applications in engineering testing and the military.

Keywords: Explosion shock wave; Mapping relation model; Finite element numerical simulation; Pressure distribution law; Static explosion test of TNT explosive.

1. INTRODUCTION

Several damage parameters, like shock waves, are generated in an ammunition explosion (Sun *et al.* 2020; Yu *et al.* 2022). Therefore, the accurate determination of the shock wave pressure distribution law is crucial for designing the ammunition and evaluating its damage power (Wang *et al.* 2021). However, the test points arranged number in actual test process is often limited. Fragments produced by ammunition explosion and flying rocks produced by shock wave will directly damage the sensor, obtaining less effective data that cannot be used to reconstruct and analyze the ammunition explosion shock wave pressure distribution law. Therefore, it is great significance to study the explosion shock wave pressure distribution law prediction model based on limited measuring point data. Additionally, it is important to calculate the surface reflection pressure and free-field pressure at different measuring point locations using the prediction model to provide accurate and reliable data support for evaluating the ammunition explosion damage power.

Presently, the reconstruction and analysis of shock wave pressure propagation distribution law during the ammunition explosion have been studied by some research groups. The results of their studies can be classified into two categories according to the reconstruction methods and principles: 1. travel time tomography for the reconstruction of pressure distribution law of shock wave, and 2. attenuation model of shock wave pressure propagation and various interpolation algorithms for the reconstruction of pressure distribution law of shock wave.

Application of travel time tomography for the reconstruction of pressure distribution law of explosion shock wave: Bai *et al.* (2014a) deployed sensors around the central explosion point to extract the shock wave travel time after the explosion, and used travel time tomography to reconstruct the pressure field. The results showed that the expectation maximization algorithm had higher reconstruction accuracy and faster speed than other algorithms and was more valuable in engineering. Based on computer tomography technology, Guo *et al.* (2014), used the weighted generalized inverse inversion algorithm to inverse the explosion shock

wave velocity field. They obtained the peak pressure field distribution according to the relationship between peak overpressure and velocity. The experimental results, within a certain test range, showed that the peak overpressure reconstruction results were better than those calculated by the empirical formula. Furthermore, Bai *et al.* (2014b) used travel time tomography to reconstruct the shock wave pressure field distribution law during the ammunition underwater explosion. A variable mesh technique was proposed to reconstruct the pressure field with a small number of sensors. However, this method had much dependencies on the location of the pressure measuring points and reconstructed shock wave propagation velocity in the actual testing process. Additionally, it required extensive calculations and had low reconstruction efficiency.

Application of attenuation model of shock wave pressure propagation and various interpolation algorithms in reconstruction of explosion shock wave pressure distribution: Lv *et al.* (2022) constructed the fitness function in the genetic algorithm based on the reflected overpressure function of the dynamic explosion ground. They determined the dynamic explosion parameters in combination with the measured overpressure and reconstructed the shock wave pressure field with the dynamic explosion overpressure function. Furthermore, Yan *et al.* (2022) combined the advantages of compression sensing in sparse constraints, used the TV regularization method to optimize the shock wave overpressure field edge information, improved the description of the internal details of the overpressure field through the dictionary learning method, and reconstructed the shock wave overpressure field with fewer data. Furthermore, Xie *et al.* (2021) analyzed the shock wave shape formation process and adopted the multi-scale wavelet decomposition method. Additionally, they gave a shock wave shape reconstruction method and compared it with the waveform obtained by the Müller-plate needle pressure sensor. The waveform reconstruction algorithm based on the multi-scale wavelet decomposition had better stability and higher accuracy. Furthermore, Yao *et al.* (2019) used the Gauss-Newton algorithm to perform nonlinear regression on the measured shock wave curve and obtained the global optimal solution of each coefficient through Zippel's interpolation algorithm. Additionally, they inverted the attenuation coefficients and overpressure peak values of unknown measuring points and reconstructed the shock wave curve. Furthermore, Yang *et al.* (2016) obtained the isobars and three-dimensional distribution of the shock wave overpressure field by using MATLAB simulation. The shock wave overpressure field reconstructed from the measured data using the B-spline interpolation algorithm was superior to the Delaunay triangulation method and the least squares method. Furthermore, Bai *et al.* (2014c) proposed an EM inversion algorithm based on prior information. The algorithm was simulated by establishing a mathematical model, and the simulation results were analyzed. The analysis results show that the inversion algorithm had higher precision and faster convergence than the traditional methods.

Therefore, this analysis shows that presently, the studies on the shock wave pressure propagation distribution law reconstruction primarily focus on refining and reconstructing the ammunition explosion shock wave pressure distribution law from the existing test data. Additionally, some researchers have studied the calculation function between the ground reflection pressure and free-field pressure from the explosion field shock wave pressure propagation characteristics perspective to improve the utilization rate of single test data. In view of these shortcomings in the current research process, it is necessary to carry out targeted research work to provide a new reconstruction method for the study of the pressure propagation distribution law.

This study, which is based on the shock wave pressure data obtained at limited measuring points during the ammunition explosion, comprehensively considered the influence of altitude and Mach reflection pressure on the shock wave pressure propagation distribution law. Furthermore, a functional mapping relationship was obtained between the ground reflection pressure and the free-field pressure. This relationship model was used to calculate the shock wave pressure and its distribution law in a certain range around the explosion center. Additionally, a static pressure test of a typical trinitrotoluene (TNT) quality of explosives was performed, and the prediction model accuracy was verified through the obtained explosion shock wave pressure data.

2. EXPLOSION SHOCK WAVE

The expansion law of the explosive products in the ammunition explosion process can be approximately considered to conform to the multi-party exponential state equation shown in Eq. (1).

$$pv^{\gamma} = const \tag{1}$$

where, p and v represent the pressure and specific volume (volume per unit mass) of the explosion products, respectively. γ represents a multi-party index, which is related to the explosive products composition and density. The value of γ increases with the increase in density. Since for a spherical charge with radius r_0, the expansion radius of explosive products after the explosion is expressed by r, the values of v and p for the explosive products are proportional to r^3 and $r^{-3\gamma}$, respectively. The value of γ is generally larger than the ideal gas isentropic index (1.4) and lies between 2 and 4.

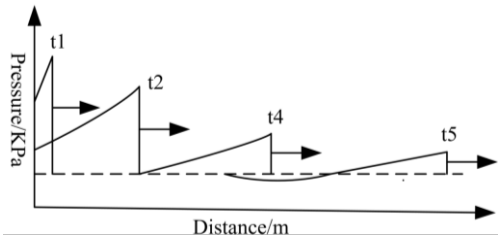

Fig. 1. Propagation process of explosion shock wave pressure.

The explosive products spread outward at a very high speed in an explosion. Consequently, the surrounding air is rapidly compressed, forming a high-pressure zone and resulting in an initial shock wave (Cheng *et al.* 2020; Mizukaki *et al.* 2020). With strong discontinuity, the initial shock wave has a large wavefront pressure and a small rear wave pressure. As a result, the head of the wave propagates at a supersonic speed. However, its tail propagates at the sound speed corresponding to the pressure. Therefore, the shock wave barotropic zone continuously widens during its propagation (Jia *et al.* 2014). The typical shock wave pressure propagation attenuation curve as shown in Fig. 1.

Parameters, such as pressure peak and propagation velocity, decrease rapidly during the explosion shock wave pressure propagation in the air since the wavefront expands with increased propagation distance. Moreover, the energy per unit area on the wavefront rapidly decreases even with no additional energy loss. Furthermore, the explosion shock wave positive pressure action zone widens with increased propagation distance, and the average energy of the unit mass air decreases with increased quantity of compressed air. Additionally, shock wave propagation is not isentropic and entropy increases on the wavefront. Wave propagation is always accompanied by irreversible energy loss due to the adiabatic compression of the air. During an explosion, the wavefront pressure attenuates rapidly at the initial stage, the pressure decay rate gradually slows down at the later stage. However, the shock wave attenuates to a sound wave when it reaches a certain distance (Du *et al.* 2014; Kong *et al.* 2022). The change in wavefront pressure with time as shown in Fig. 2 (Tanaka *et al.* 2018).

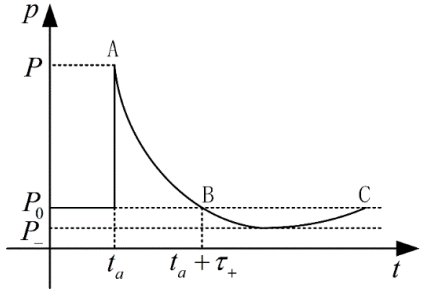

Fig. 2. Pressure attenuation process in the propagation of a shock wave.

When the shock wave propagates without boundary body, it propagates as a spherical wave. Since the pressure on its wavefront is equal at equal distances from the explosion center, the shock wave pressure spatial isobaric line is a sphere. The shock wave launches on the obstacle surface when it encounters obstacles, like ground and fixed walls, during its propagation. The functional relationship between the reflected and incident shock wavefront pressures p_2 and p_1, respectively, is given in Eq. (2).

$$\frac{p_2}{p_1}=\frac{(3\gamma-1)p_1-(\gamma-1)p_0}{(\gamma-1)p_1-(\gamma+1)p_0} \tag{2}$$

where, γ and p_0 represent the adiabatic index and initial pressure of air, respectively. p_0 can be ignored when the incident shock wave pressure p_1 is much greater than it ($p_1 \gg p_0$). The above functional relationship can be simplified as shown in Eq.(2).

Generally, $\gamma = 1.4$, so $p_2 / p_1 = 8$. However, when the air is compressed by a strong shock wave, γ decreases, resulting in an increase in the reflection pressure. For example, $p_2 = 13p_1$ for $\gamma = 1.2$ and $p_2 = 23p_1$ for $\gamma = 1.1$. Subsequently, it can be concluded that the reflection of the wave will enhance the explosion shock wave damage efficiency on the target when the strong shock wave is normal to the target. Therefore, it is great significance to study the free-field pressure and surface reflected pressure distribution law to clarify the shock wave pressure propagation and distribution law.

3. SHOCK WAVE PRESSURE DISTRIBUTION LAW PREDICTION MODEL BASED ON LIMITED MEASURING POINT DATA

3.1 Functional Correspondence between Altitude and Atmospheric Pressure

The influence of altitude and ambient temperature on air density is yet to be considered in the studies which have calculated blast wave pressure in an explosion field. Nevertheless, studies have determined that air density has a very significant effect on the shock wave pressure propagation. Specifically, at lower air densities (at higher altitudes), the shock wave pressure obtained at the measuring points at the same distance from the explosion center under the same explosion condition is lower, and the shock wave front propagation speed is higher. According to a theoretical analysis in aerodynamics, the functional relationship between altitude H (in m) and gas pressure P_x is as follows (Deng 2019):

$$P_x = P_0 \times (1 - H / 44300)^{5.256} \tag{3}$$

where, $P_0 = 101.352\ KPa$,is the standard atmospheric pressure. The functional relationship between air density ρ_x and P_x is as follows

(Chen *et al.* 2022; Pang *et al.* 2018):

$$\rho_x = \frac{P_x}{P_0}\rho_0 \tag{4}$$

The air densities at different altitudes can be calculated by introducing Eq. (3) into Eq. (4) as follows:

$$\rho_x = \frac{P_0 \times (1 - H / 44300)^{5.256}}{P_0}\rho_0 \tag{5}$$

The air density at standard atmospheric pressure $\rho_0 = 1.293\ kg / m^3$.

In addition to the influence of altitude, ambient temperature is an important factor affecting air density. Therefore, by introducing the influence of ambient temperature on air density, Eq.(5) can be expressed as follows:

$$\rho_x = \frac{P_0 \times (1 - H / 44300)^{5.256}}{P_0}\rho_0 \times (\frac{273.15}{T}) \tag{6}$$

Where, T is the absolute temperature under the actual environment (in K). Absolute temperature = temperature in Celsius + 273.15 and 273.15 K is 0 °C. Therefore, the functional formula between ρ_x, H, and actual ambient temperature T_1 can be expressed as follows:

$$\rho_x = \frac{P_0 \times (1 - H / 44300)^{5.256}}{P_0}\rho_0 \times (\frac{273.15}{T_1 + 273.15}) \tag{7}$$

3.2 Mapping Function between the Surface Reflected Pressure and Free Field-Shock Wave Pressure

Presently, the explosion shock wave pressure is commonly calculated using a large number of experimental data along with a similarity theory like the Sadovsky formula. Furthermore, these are applicable to the shock wave pressure generated calculation by TNT explosive explosion in unbounded space (Sadovskyi 1952). The overpressure at different altitudes can be calculated by introducing Eq. 8 which considers the influence of altitude in calculating shock wave pressure. The functional relationship is shown as follows:

$$\Delta P_{ms} = a_1 \times \frac{\sqrt[3]{\omega}}{r}(\frac{p_h}{p_0})^{2/3} + a_2 \times (\frac{\sqrt[3]{\omega}}{r})^2 (\frac{p_h}{p_0})^{1/3} + a_3 \times (\frac{\sqrt[3]{\omega}}{r})^3 \tag{8}$$

where, ΔP_{ms}, ω, r, and $\bar{r} = r / \sqrt[3]{\omega}$ denote free-field shock wave overpressure peak during infinite air explosion (in MPa), TNT charge (in kg), distance between measuring point and explosion center (in m), and explosion proportional distance (in $m / kg^{1/3}$), respectively. p_h and p_0 denote the atmospheric pressures at the local altitude and sea level (in MPa), respectively. a_1, a_2, a_3 are the undetermined coefficients.

Furthermore, Eq. 8 is used to calculate the free-field pressure peak for ground explosions occurring at different altitudes. Generally, the actual ground test process employs the explosion height. The test results will be affected by the Mach wave when the shock wave incident angle at the test point is greater than the Mach reflection critical angle (40°) (Cheng *et al.* 2011). The obtained surface reflection pressure value at this time was the pressure of the Mach bar. Therefore, a correction coefficient of the shock wave incident angle must be introduced in Eq. 8 to convert the surface reflection pressure into the Mach rod pressure while calculating the surface reflection pressure under the Mach wave influence, as follows:

$$\Delta P_{ground} = \Delta P_{ms} \times (1 + \cos\varphi_0) \tag{9}$$

Where, ΔP_{ground} and φ_0 denote the peak overpressure measured by the ground reflection pressure sensors (in MPa) and the shock wave incident angle, respectively. φ_0 is calculated as follows:

$$\varphi_0 = \arctan(r / H) \tag{10}$$

According to this analysis, the functional relationship between the surface reflection pressure and free-field pressure in ammunition explosion process can be expressed as follows:

$$\begin{cases} \Delta P_{ms} = a_1 \times \frac{\sqrt[3]{\omega}}{r}(\frac{p_h}{p_0})^{2/3} + a_2 \times (\frac{\sqrt[3]{\omega}}{r})^2 (\frac{p_h}{p_0})^{1/3} + a_3 \times (\frac{\sqrt[3]{\omega}}{r})^3 \\ \Delta P_{ground} = \Delta P_{ms} \times (1 + \cos\varphi_0) \end{cases} \tag{11}$$

Subsequently, Eq. 11 is used for the nonlinear adaptive fitting analysis with respect to the surface reflected pressure and free-field shock wave pressure data obtained from the finite element numerical simulation and the actual test to predict the actual explosion shock wave pressure distribution law. Thus, the established shock wave pressure calculation function coefficients a_1, a_2, a_3 are obtained.

Furthermore, the free-field pressure and the surface-reflected pressures peak values at the location where the measuring point radius exceeds the Mach reflection limit radius were calculated using ΔP_{ms} and ΔP_{ground} in Eq. 11, respectively. Therefore, the combination of the two functional relations can help to achieve the peak data of the surface-reflected and free-field shock wave pressures within a certain range of the explosion center. Furthermore, the shock wave pressure distribution law during the ammunition explosion can be reconstructed based on this data.

Most testing processes use explosives other than

TNT, such as thermobaric, cloud, and aluminized explosives. The equation calculation accuracy will be significantly reduced due to the type of explosive. Therefore, it necessitates first to use the ground reflection or free-field pressure data collected in the test process to conduct an inverse calculation using Eq. 11 and obtain the TNT explosive equivalent quality of the ammunition for reconstructing the pressure distribution law of an ammunition explosion. Next, the TNT explosive equivalent mass must be used to obtain the shock wave pressure data at different measuring points in the explosion field. Finally, the shock wave pressure distribution is reconstructed.

3.3 Shock Wave Pressure Finite Element Numerical Simulation Analysis

The finite-element numerical simulation analysis of the explosion shock wave pressure distribution and propagation laws for TNT was conducted to obtain the surface-reflected and free-field shock wave pressure data at different measuring points and the undetermined coefficients in the prediction model. The display dynamics simulation software, AUTODYN, was used to build a numerical simulation model with a ratio of 1:1 with the testing environment in the shooting range and simulate the explosion environment of real ammunition in a shooting range to the greatest extent. The process for establishing the model included material selection, mesh generation, solver setting, and detonation mode setting. The proposed finite element numerical simulation model is shown in Fig. 3. The air space dimensions were 10000 mm × 5000 m (length × width), with a mesh size of 10 mm × 10 mm and Euler grid type. The other three boundary conditions, except the axis of symmetry, were set as pressure outflow to simulate that the boundary pressure does not reflect in the actual environment. The dimensions of the ground material, sandy soil, was 10000 mm × 1500 mm (length × width) with a mesh size of 10 mm × 10 mm and Lagrange grid type. The state equation for TNT was the Jones-Wilkins-Lee (JWL) state equation. Additionally, the explosive mass was 41 kg, the ratio of explosive length to diameter was 1:1, and the calculated explosive radius was 200 mm. The TNT explosive center was 2000 mm above the ground. Furthermore, the TNT initiation mode was the center point initiation. Additionally, it was necessary to set the free-field shock wave and the ground-reflected pressure monitoring points at the same height as the explosion center and on the surface, respectively, to obtain the shock wave pressure variation curves with explosion time at different measuring points during the ammunition explosion. In Fig. 3, 1~19 and 20~39 represent the ground-reflected and free-field shock wave pressure measuring points, respectively.

In the finite element numerical simulation model, the air is described by ideal gas state equation. The state equation is based on Boyle's law and Guy Lussac's law, which suitably for describe the change laws of various moving gases. The state equation for an ideal gas is shown in Eq. (12).

$$p = (\gamma - 1)\frac{\rho}{\rho_0}E_0 \tag{12}$$

where, p, γ, and E_0 represent air pressure, adiabatic index, and initial specific internal energy of air, respectively. ρ and ρ_0 represent air densities after compression or expansion and initially, respectively. The value of each parameter as shown in Table 1.

The TNT explosive explosion process described by JWL state equation, which is shown in Eq. (13). (Wang *et al.* 2016; Yang *et al.* 2007)

$$P = A\left(1-\frac{\omega}{R_1V}\right)e^{-R_1V} + B\left(1-\frac{\omega}{R_2V}\right)e^{-R_2V} + \frac{\omega}{V}E \tag{13}$$

Table 1 The values of parameters in the equation of state for ideal gas.

ρ_0 (kg/m^3)	γ	E_0 (J/kg)
1.225	1.4	2.068×10^5

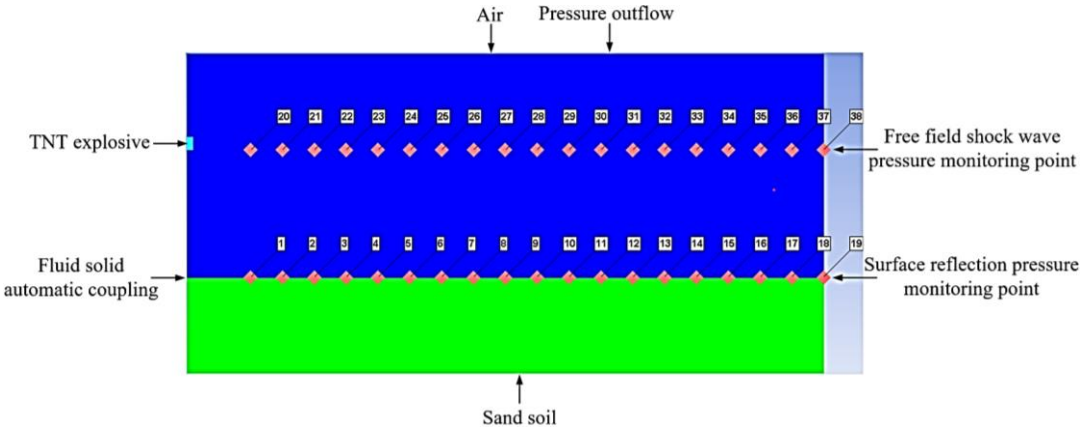

Fig. 3. Finite-element numerical-simulation model of explosion shock wave pressure.

Table 2 Values of parameters in JWL equation of state.

A(Pa)	B(Pa)	R_1
3.712×10^{11}	3.23×10^{9}	4.15
R_2	ω	E
0.95	0.3	4.29×10^{6}

where, P, V, and E represent pressure, volume, and internal energy, respectively. A and B are material parameters. R_1, R_2, and ω are constants. The values of the parameters are shown in Table 2 (Taylor *et al.* 2019).

The explosion shock wave pressure finite-element model was used to obtain the shock wave pressure evolution cloud diagram and the pressure change curve with time during the explosion. Several cloud images and pressure time history curves were obtained. The pressure evolution cloud diagram under partial explosion is shown in Fig. 4. The pressure-time history curves of the ground-reflected and free-field shock waves are shown in Fig. 5 and 6, respectively.

As shown in Fig. 4 (a) and (b), in the shock wave pressure evolution cloud diagram, the shock wavefront propagated forward in a spherical wave form at the ammunition explosion initial moment. Additionally, the front and the rear ends of the wavefront were high- and low-pressure (rarefied) areas, respectively. With the explosion time passage, the incident shock wave front collided with the ground, and a reflected shock wave was formed at the collision interface, as shown in Fig. 4 (c), the reflected shock wavefront brightness was much higher than that of the incident shock wave front brightness. Therefore, the reflected shock wave pressure was significantly higher than the incident shock wave pressure. Additionally, since the reflected shock wave front propagation speed was greater than that of the incident shock wave front, it will catch up with the incident shock wave at a certain explosion time, forming a Mach wave at their intersection. Since the Mach wave propagates forward perpendicular to the ground, it is called a Mach rod. The incident shock wave, reflected shock wave, and Mach wave intersection is called the three-wave point, as shown in Fig. 4 (d). Since the speed of reflected shock wave is faster, the three-wave point track height will gradually increase with the passage of the explosion time, and the track height change curve will approximately meet the exponential function, as shown in Fig. 4 (e) and (f). In the process of ammunition explosion shock wave

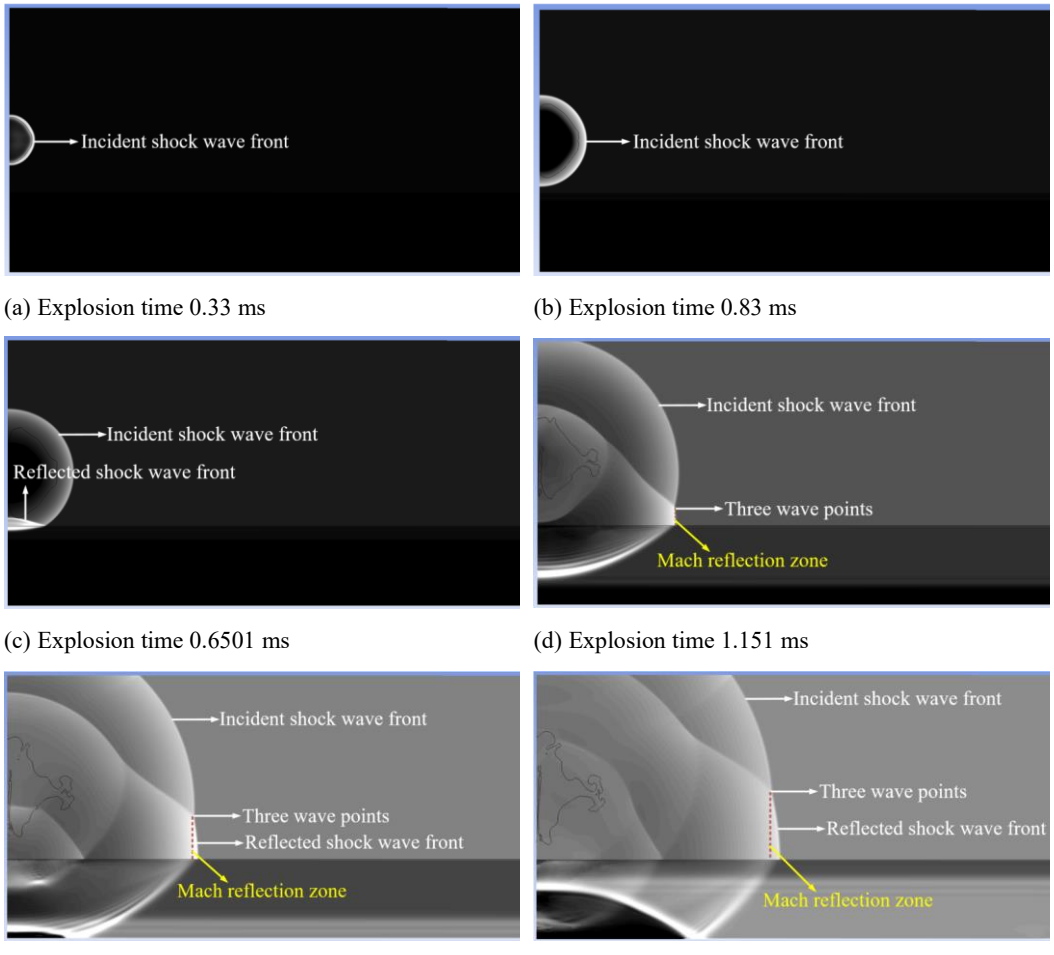

(a) Explosion time 0.33 ms

(b) Explosion time 0.83 ms

(c) Explosion time 0.6501 ms

(d) Explosion time 1.151 ms

(e) Explosion time 1.400 ms

(f) Explosion time 2.400 ms

Fig. 4. Cloud chart of shock wave pressure evolution at different explosion times.

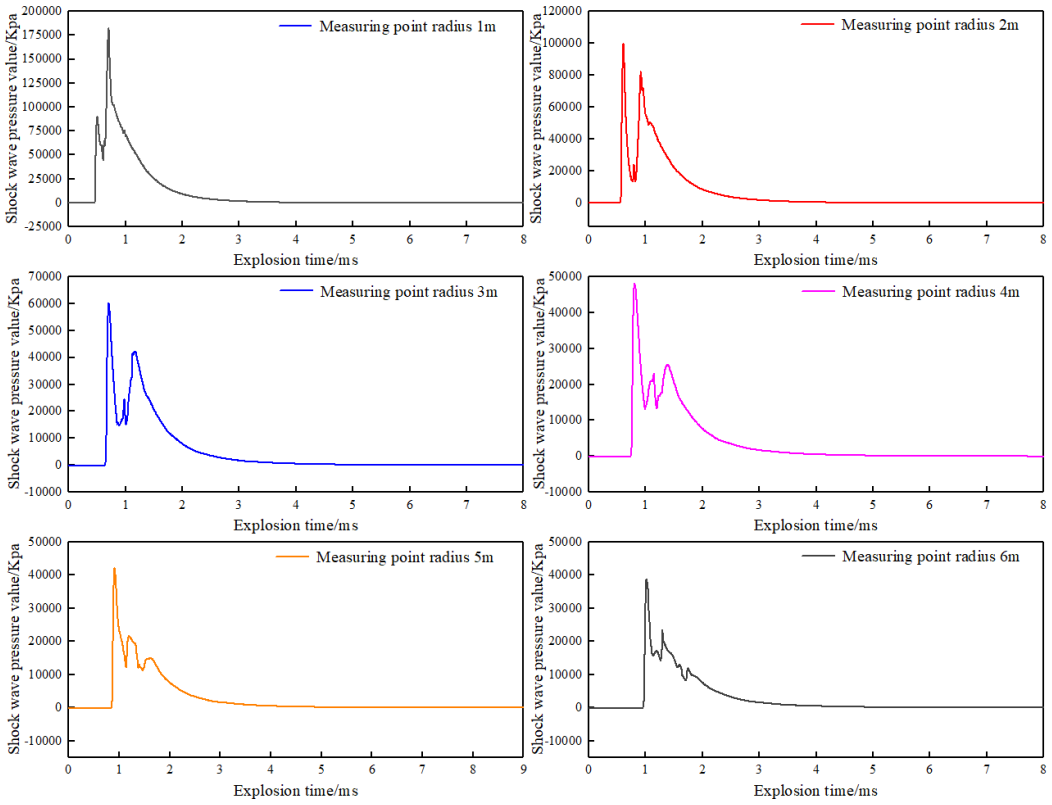

Fig. 5. Pressure-time history curve of ground-reflection.

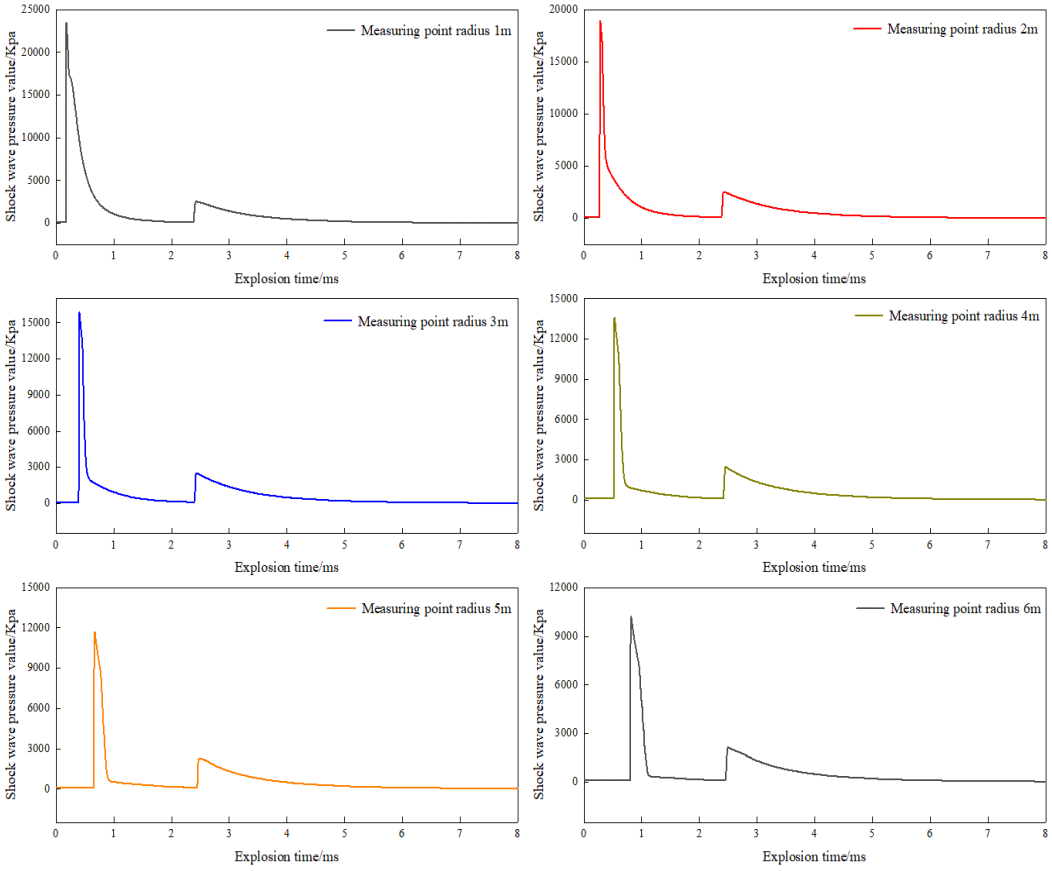

Fig. 6. Pressure-time history curve of the free-field shock wave.

pressure test, free-field shock wave pressure refers to the incident shock wave pressure. According to the change rule of the three wave point track height, in the actual engineering test, the installation height of the free field shock wave pressure sensor should gradually increase with the increase of the distance between the test point and the explosion center. Only when the sensor installation position is above the three wave point can the accurately obtained the incident shock wave pressure.

The finite element numerical simulation analysis of the shock wave pressure under different TNT explosive qualities was conducted using the obtained finite-element numerical simulation model. Furthermore, the obtained pressure data was used to perform nonlinear adaptive fitting on Eq. 11, resulting in the functional relationship equation, Eq. 11, where a_1 = 0.084, a_2 = 0.27, and a_3 = 0.7. Therefore, Eq. 11 can be expressed as follows:

$$\begin{cases} \Delta P_{ms} = 0.084 \times \dfrac{\sqrt[3]{\omega}}{r}\left(\dfrac{p_h}{p_0}\right)^{2/3} + \\ 0.27 \times \left(\dfrac{\sqrt[3]{\omega}}{r}\right)^2 \left(\dfrac{p_h}{p_0}\right)^{1/3} + 0.7 \times \left(\dfrac{\sqrt[3]{\omega}}{r}\right)^3 \\ \Delta P_{ground} = \Delta P_{ms} \times (1 + \cos\varphi_0) \end{cases} \tag{14}$$

4. Typical TNT Explosives Static Explosion Shock Wave Pressure Test

TNT explosives were used to conduct a typical static explosion test to verify the shock wave pressure distribution prediction model accuracy. The mass and length-to-diameter ratio of the TNT explosive were 10 kg and 1:1, respectively. The warhead was placed on the ammunition carrier, and the explosive was placed at a height of 2 m from the ground during the test. The test setup as shown in Fig. 7.

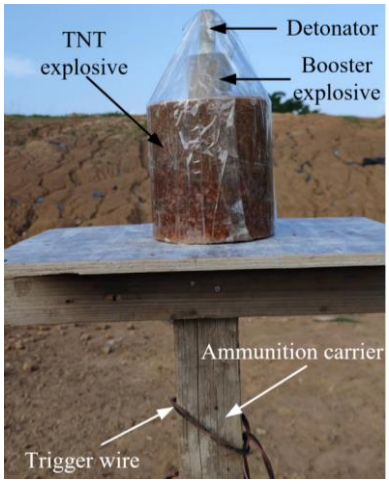

Fig. 7. TNT explosive placement mode.

The explosive structure mainly comprised the detonator, booster, and TNT explosive. The detonator was inserted into the booster, which contacts the upper surface of the TNT. The detonator was detonated by electric firing during the test. The detonator ignites the booster, which detonates the TNT explosive, completing the detonation process.

Furthermore, multiple shock wave pressure sensors were set up at different measuring points within the explosion center radii to obtain maximum ground-reflected and free-field pressure data during the TNT explosion. The ground-reflected and free-field shock wave pressure measuring points layouts during the actual test are shown in Fig. 8 and Fig. 9, respectively.

Furthermore, a shock wave pressure measuring system was devised to accurately obtain the data of the ground-reflected and free-field shock wave pressures during the explosion, as shown in Fig. 10. A 113 B piezoelectric pressure sensor (American PCB Company) and a pen-shaped piezoelectric pressure sensor (Swiss Kislter company) were used as the surface-reflected and the free-field shock wave pressure sensors, respectively. TranNET 308S (ELSYS Corp.) was used as the data collector. Additionally, a self-developed multi-channel and high-precision synchronous trigger was used to

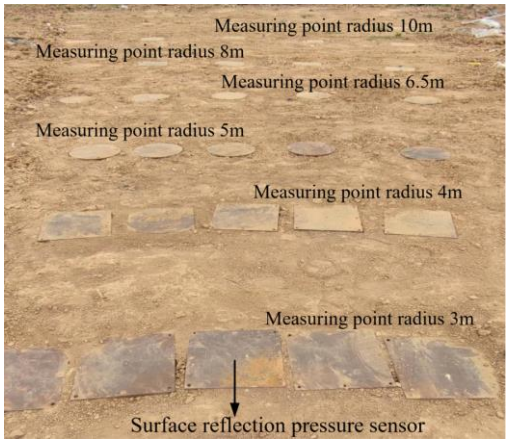

Fig. 8. Field layout of the ground-reflected pressure sensor.

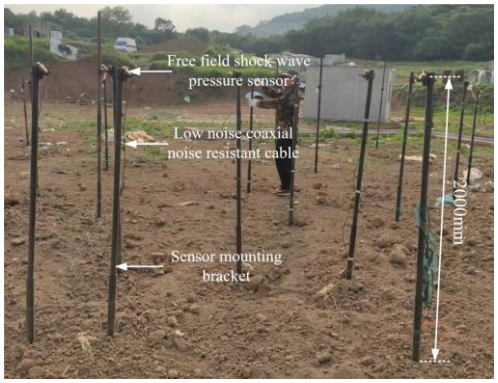

Fig. 9. Field layout of the free-field shock wave pressure sensor.

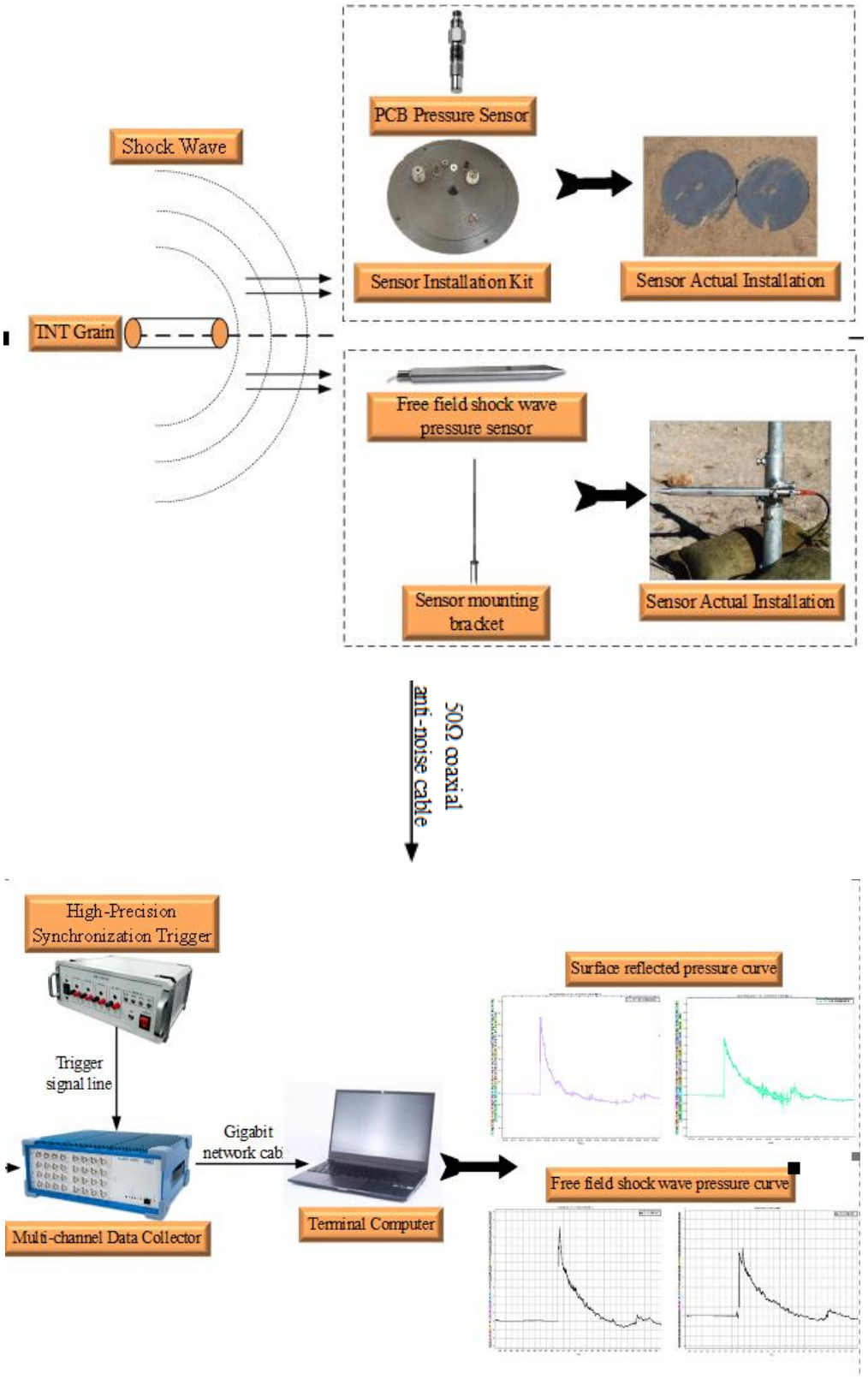

Fig. 10. Explosion shock wave pressure-measuring system.

provide a unified trigger time benchmark for data acquisition system.

As shown in Fig. 10, the surface reflection pressure sensor and the free-field pressure sensor are piezoelectric pressure sensors with built-in ICP preamplifier circuit. The surface reflection pressure sensor rise time is $\leq 2\ \mu s$, the nonlinearity is $\leq 1.0\%$ FS, the temperature sensitivity coefficient is $\leq$

0.06%/° F, and the maximum impact is 20000 g pk. The free-field pressure sensor rise time is ≤ 6.5 μs , the temperature sensitivity coefficient is ≤ 0.05% FS, the resonance frequency is ≥ 400kHz, and the output impedance ≤ 100 Ω. In order to adapt to the test environment of the range, the data collector selects TranNET 308S portable data acquisition instrument. The data collector can simultaneously realize data acquisition of 32 channels, with a working bandwidth of ≥4MHz, input noise < 0.03 mV rms at a sampling rate 1 MS/s, and resolution of 14 bits and 16 bits . The instrument also has two trigger acquisition modes: external trigger and internal trigger. The high-precision synchronous trigger controller can output ± 5 V square wave pulse signal from 24 channels at the same time. In the data acquisition process, it is necessary to ensure that each channel trigger time reference of the collector is highly consistent, so each channel output signal synchronization time delay of the synchronous trigger instrument needs to be less than 1 μs. The data transmission and communication between the data collector and the terminal computer are connected via gigabit Ethernet (gigabit network cable is required), which improves collected data transmission efficiency and can realize the efficient transmission of a large number of shock wave pressure data under the collector continuous acquisition state.

Furthermore, from the large number of measuring points set in the actual testing process, a few surface-reflected pressure signals were selected for display, as shown in Fig. 11.

As per the obtained measured and simulated data, the change laws of the finite element numerical simulation and measured shock wave pressure-time history curve were consistent. Additionally, a few shock wave pressure signals had two peaks, indicating the effect of the Mach wave on them. The first and the second peaks represent the incident and reflected shock wave pressures, respectively. Therefore, the finite element numerical simulation model proposed in this study was feasible, and the Mach rod influence on the shock wave propagation law must be considered in constructing the prediction model.

Furthermore, the peak surface-reflected pressure obtained for 10 kg TNT explosive and 4, 5, 6.5, 8, 10, 12, and 15 m distances between the measuring point and the explosion center were compared with the peak surface-reflected pressure data obtained from the static explosion test to verify the calculation results accuracy of the finite element numerical simulation model for the shock wave pressure propagation and distribution in the explosion field. The measured shock wave pressure peak value at different measuring points, the change curve, and the relative error results for the shock wave pressure peak value obtained by numerical simulation are shown in Fig. 12.

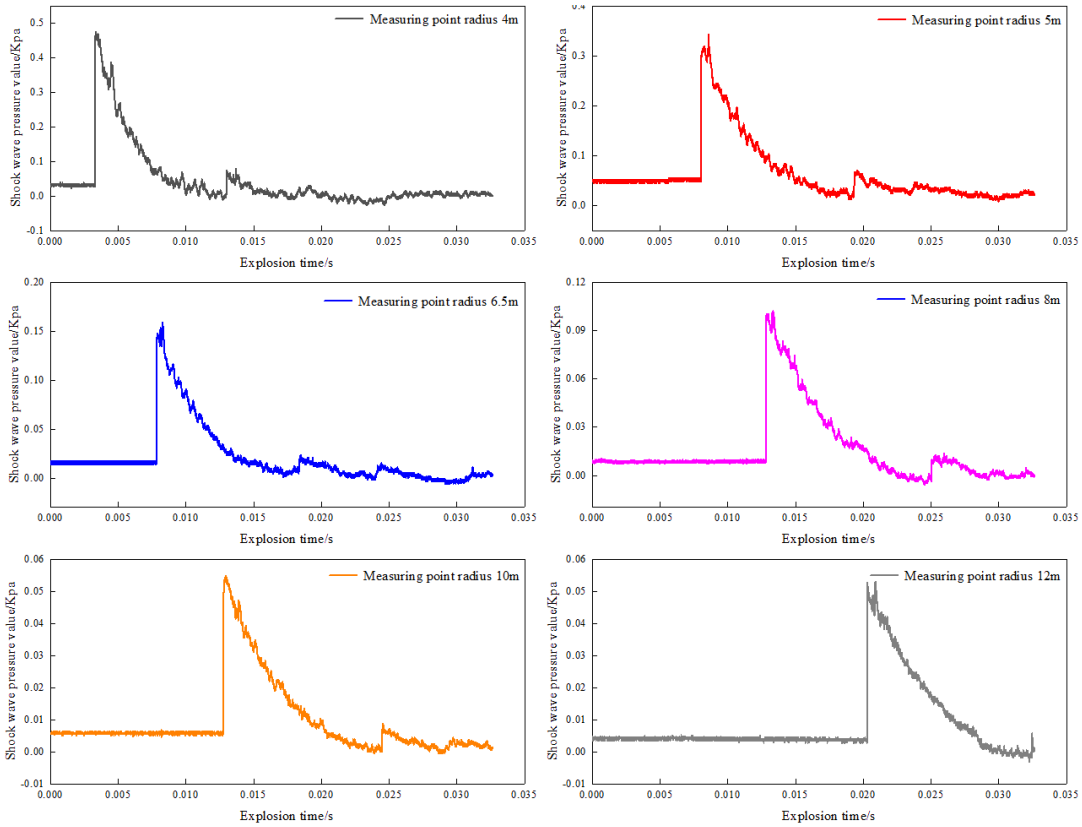

Fig. 11. Pressure-time history curve of the measured surface-reflected pressure.

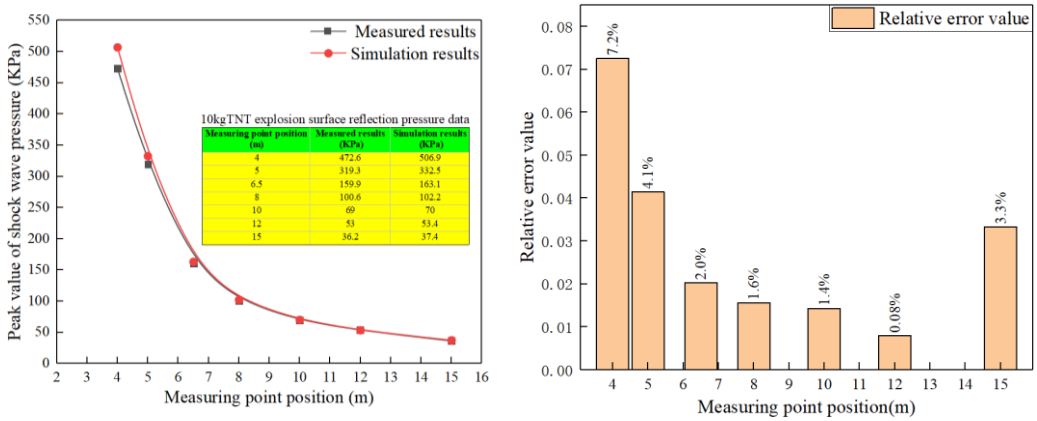

(a) Shock wave pressure peak change curve (b) Pressure peak relative error histogram

Fig. 12. Comparison results between the numerical simulation and measured peak surface reflection pressure data.

The comparative analysis of the surface reflected pressure peak data shows that for 10 kg TNT explosive, the measured and the finite element numerical simulation shock wave pressure peak values were highly consistent with the pressure peak value attenuation law for increased distance between the measuring point and the explosion center, as shown in Fig. 12(a). The pressure peak value quantitative analysis at different measuring points showed that the maximum relative error of 7.2% between the measured and finite element numerical simulation results occurred at a distance of 4.0 m between the measuring point and the explosion center. Additionally, the minimum relative error of 0.08% occurred at a distance of 12.0 m between the measuring point and the explosion center. The pressure peak value relative errors at other measuring points were between them, as shown in Fig. 12 (b). The pressure peak value relative error increased with the distance between the measuring point and the explosion center decreased. Because in the actual test process, the pressure distribution law at the explosion center is affected by the loading density, shape, initiation method, etc. of TNT explosive, which leads to the pressure complex distribution law. The measured surface-reflected pressure data is quite different from the finite element numerical simulation data. However, the pressure peak overall change law is consistent. Therefore, the finite element numerical simulation results accuracy met the explosion field damage test requirements, and the finite element numerical simulation model established can be used to analyze the pressure propagation distribution law during the ammunition explosion process.

Furthermore, the measured explosion shock wave overpressure curve peak value was extracted, and the shock wave pressure peak value at the corresponding measuring point was calculated using the prediction model to conduct a quantitative analysis of the obtained explosion shock wave pressure data. The extracted and the prediction model-based pressure peaks are shown in Fig. 13. The relative error in the figure was calculated using Eq. (15).

$$\varphi = \frac{P_{\text{Measured value}} - P_{\text{Calculated value}}}{P_{\text{Measured value}}} \times 100\% \tag{15}$$

The measured shock wave pressure peak value at different measuring points was compared with the value calculated using the prediction model. The prediction model was used to calculate the shock wave pressure peak value for 10 kg TNT explosive and the distance in the range of 4 m–15 m between the measuring point and the explosion center. The maximum relative error of 15.8% occurred at a distance of 10 m. The minimum relative error of 8.9 % occurred at a distance of 6.5 m. Moreover, the relative error in the calculation results at other measuring points was less than 16%. Therefore, the prediction results were greater than the measured shock wave pressure peak value since the part of data used for fitting is obtained through finite element numerical simulation when the coefficients a_1, a_2, and a_3 in the established prediction model are fitted nonlinearly. Additionally, since this simulation method was relatively ideal compared with the actual test environment of the shooting range, and there were fewer interference factors in the shock wave propagation process, the shock wave pressure peak value obtained through the simulation will be slightly larger, resulting in more significant prediction results.

Therefore, in subsequent studies, more tests can be conducted on the ammunition explosion shock wave pressure, and the obtained test data can be used to modify our proposed prediction model, improving its calculation accuracy. Nevertheless, in terms of overall calculation accuracy, the prediction model can favorably calculate the shock wave pressure peak value in the ammunition explosion

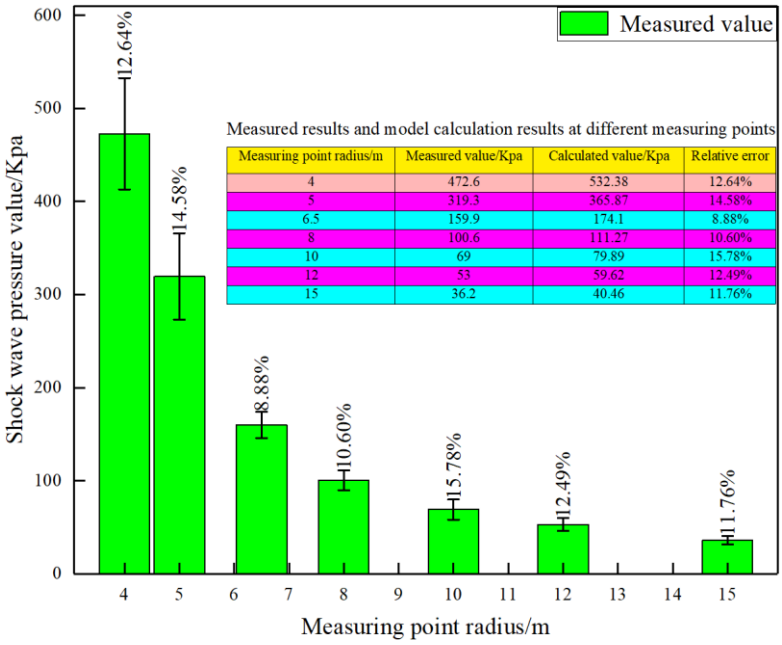

Fig. 13. Measured results and the prediction model-based results at different measuring points.

process, and the calculation results were highly consistent with the measured results. Furthermore, the prediction accuracy meets the shock wave pressure peak value calculation accuracy requirements in the explosion field engineering tests. Therefore, the shock wave pressure time-space distribution prediction model in the explosion field can be applied for calculating the pressure peak value, providing scientific data support for evaluating the ammunition explosion damage power, and guiding ammunition design.

5. CONCLUSIONS

Based on the limited measuring points shock wave pressure data and the altitude influence on its distribution law, the study established the functional mapping relationship between the surface-reflected and free-field shock wave pressures. Additionally, the finite element numerical simulation of the typical TNT explosives quality and the static explosion test shock wave pressure were performed. The results showed that established prediction model of the explosion shock wave pressure distribution law in this study well interpreted the test data. The maximum and minimum relative errors of the prediction model-based calculation results were 15.8% and 8.9%, respectively. The prediction model overall calculation accuracy was 84%. The prediction model calculation accuracy met the requirements for the calculation accuracy of the explosion shock wave peak pressure in engineering tests. Therefore, the prediction model can provide reliable data support for evaluating the ammunition explosion damage power and has significant application value for engineering tests of explosion shock wave pressure.

ACKNOWLEDGMENTS

This work was funded by National Natural Science Foundation of China, project number: 11372143.

REFERENCE

Bai, M. M., Y. L. Guo, F. Wang and L. M. Wang (2014a). Reconstruction of underwater explosion shock wave overpressure field based on variable grid . *Tactical Missile Technology* (04), 105-110.

Bai, M. M., Y. L. Guo and L. M. Wang (2014b). Explosive overpressure field reconstruction technology based on EM algorithm. *Journal of Missile, Arrow and Guidance* 34 (03), 187-190.

Bai, M. M., Y. L. Guo and L. M. Wang (2014c). Reconstruction algorithm and comparison of overpressure field of underwater explosion shock wave . *Journal of Missile, Arrow and Guidance* 34 (06), 71-74.

Chen, L. M., Z. B. Li, R. Chen and D. X. Zou (2022). Experimental study on propagation characteristics of explosion shock wave in plateau environment. *Explosion and Shock* 42 (05), 114-124.

Chen, X. F., X. C. Huang, Q. B. Dou (2020). Calculation method of explosion shock load in engineering analysis. *Strength and Environment* 47(01), 26-32.

Chen, X. W., J. X. Wang, K. Tang, R. M. Cheng and L. Zhou (2019). Shock initiation test and simulation of near-field explosion shock wave

on shielded press mounted TNT. *Journal of High Voltage Physics* 33 (01), 127-134.

Cheng, F. S., P. Song, X. H. Gu, G. Nian and X. X. Zeng (2011). Numerical study on propagation and reflection of TNT charge explosion wave above rigid plane. *Blasting Materials* 40 (04), 1-4

Deng, G. Q. (2019) Analysis on the influence of altitude on air shock wave parameters of conventional explosion. *Protection Engineering* 41 (03), 26-32.

Du, H. M., X. Y. Cao, Z. W. He and L. Xu (2014). Analysis and verification of air and ground shock wave characteristics of near-ground explosion. *Journal of Projectiles, Rockets, Rockets and Guidance* 34(04), 65-68.

Guo, Y. L., Y. Han and L. M. Wang (2014). A reconstruction method of shock wave overpressure field based on generalized inverse algorithm. *Explosion and Shock* 34 (06), 764-768.

Jia, Y. F., C. Q. Zhang and J. Kang (2014). Explosion shock wave signal test and wavelet analysis. *Journal of Projectiles, Rockets and Guidance* 34(05), 86-89.

Kong, X. F., L. Q. Wang, T. Yu, Z. He, H. Luo and B. M. Li (2022). Free-field shock wave test method for meteorological air cannons. *Measurements* 189,110456.

Lv, Z. J., T. Y. Li Ha, C. Y. Gao, X. L. Zhu and F. L. Huang (2022). Dynamic explosion overpressure field reconstruction method based on ground reflected shock wave and genetic algorithm. *Journal of Safety and Environment* 22 (04), 1872-1878.

Mizukaki, T., A. Kato and M. Mori (2020). Fundamental study on blast simulator for blast injury research. *Science and Technology of Energetic Materials* 81(1),17-23.

Pang, C. Q., G. Tao, P. J. Zhou, Q. Fang and L. Liu (2018). An effective prediction method of explosion shock wave parameters in plateau environment. *Vibration and Shock* 37 (14), 221-226.

Sadovskyi, M. A. (1952). *Mechanical Action of Air Shock Waves of Explosion, Based on Experimental Data*. Moscow, lzd Akad Nauk SSSR.

Sun, Z., X. Miao and C. Jagadeesh (2020). Experimental investigation of the transonic shock wave/boundary-layer interaction over a shock-generation bump. *Physics of Fluids* 106102.

Tanaka, K., T. Watanabe, K. Nagata, A. Sasoh, Y. Sakai and T. Hayase (2018). Amplification and attenuation of shock wave strength caused by homogeneous isotropic turbulence. *Physics of Fluids* 30(3), 035105.

Taylor Marcus, K., M. Hernández Lisa, J. Stump, and T. Jeremy (2019). Blast exposure interacts with genetic variant 5HTTLPRto predict stress symptoms in military explosives personnel. *Psychiatry research* 280.

Wang, F. and Y. Q. Bai (2016). Shock wave overpressure field reconstruction technology based on OSEM algorithm. *Shanxi Electronic Technology* (01), 15-18.

Wang, L. Q., F. Shang, J. W. Zhang and D. R. Kong (2021). Numerical simulation experiment research on damage power of high explosive. *Journal of Testing Technology* 35 (01), 6-11.

Xie, Y. C., H. B. Zhou, Y. Tao, Y. Tao and C. X. Wang (2021). Research on the reconstruction method of underwater electric explosion shock wave shape based on wavelet decomposition. *Vibration and Shock* 40 (05), 149-153+178.

Yan, X. L., J. Li, H. H. Kong, L. M. Wang and Y. L. Guo (2022). Shock wave overpressure field reconstruction method based on compression sensing. *Electronic Measurement Technology* 45 (02), 84-90.

Yang, X., S. Q. Shi, P. F. Cheng, and J. Pang (2007). Empirical formula comparison and numerical simulation of the propagation law of explosion shock wave in air. *Sichuan Architecture* 27 (5), 71-73.

Yang, Z., Z. J. Zhang and Y. L. Xia (2016). Shock wave overpressure field reconstruction based on B-spline interpolation fitting. *Science, Technology and Engineering* 16 (07), 236-240.

Yao, Y., Y. H. Ding, D. X. Pei, and X. G. Zhang (2019). Reconstruction method of shock wave curve of explosion in air. *Journal of Metrology* 40 (04), 636-641.

Yu, Y. H., R. Guo, P. Song, X. H. Gu and H. W. Hu (2022). Study on overpressure characteristics of underwater two-point explosion shock wave of aluminized explosives. *Journal of Underwater Unmanned Systems* 30 (03), 300-307.